Model-Based Control of Brake Mean Effective Pressure in a Euro 6 1.6L Diesel Engine Featuring Multi-after Injection Patterns

Roberto Finesso,[1] Omar Marello,[1] Ezio Spessa,[1] Vincenzo Alfieri,[2] Adriana Colaiemma,[2]
Gabriele De Matteis,[2] and Luca Scavone[2]
[1]Politecnico di Torino, Italy
[2]Punch Torino S.p.A., Italy

Abstract

A real-time model-based approach for the control of BMEP (Brake Mean Effective Pressure) has been developed and assessed for a Euro 6 1.6L GM diesel engine. The model provides the fuel quantity necessary to achieve a desired BMEP target. The engine features complex injection patterns, including pilot, main and multi-after injections.

The approach is based on the use of feed-forward ANNs (artificial neural networks), which have been trained using virtual tests simulated by a previously developed, low-throughput, mean-value, physical combustion model.

The physical combustion model is based on an improved version of the accumulated fuel mass approach, and is capable of predicting the heat release and the in-cylinder pressure. The latter quantity is in turn used to extract the IMEP (Indicated Mean Effective Pressure). The BMEP is then obtained from the IMEP, while taking into account the friction and accessory-related contributions. A novelty of this study is the assessment of the low-throughput physical combustion model for complex injection patterns, including not only pilot and main shots, but also multi-after pulses.

The physical model and the ANN-based model have been assessed considering experimental data acquired at the GM-GPS (General Motors – Global Propulsion Systems) facilities, under steady-state and transient conditions, over several driving cycles.

Introduction

The need to comply with the increasingly stringent pollutant emission regulations (such as the current Euro 6d limits in Europe) and CO_2 emission constraints (the EU fleet-wide average emission target for new cars will be 95 gCO_2/km to be reached by 2021) has led to a growth in the complexity of the engine hardware and software.

Some of the recent trends which may produce remarkable benefits for both pollutant and CO_2 emissions include engine downsizing [1], alternative fuels, such as CNG (Compressed Natural Gas) and biofuels [2], innovative combustion concepts, such as HCCI (Homogeneous Charge Compression Ignition) and PCCI (Premixed Charge Compression Ignition) [3], advanced high-pressure common rail systems [4-5], innovative combustion controls [6-13] and powertrain electrification [14-16].

Interest in model-based combustion control has been growing in the last few years, due to the increasingly high performance of ECUs (engine control units). Model-based combustion controllers offer several advantages over the traditional map-based approach, such as a reduction in the experimental effort required for calibration, the possibility of setting and achieving the desired combustion parameter (e.g., brake mean effective pressure) and pollutant emission targets (e.g., engine-out NOx) in real-time, and the potential of being integrated with emerging V2X (vehicle-to-everything) technologies.

Model-based combustion controllers are interesting, especially for diesel engines, which are characterized by a higher degree of complexity than spark-ignition ones. Although the current social and political attitude towards diesel technology is negative, it should be pointed out that recent innovations have led to a dramatic reduction in NOx emissions, far below those set in European standards for after 2020 [17]. Moreover, the diesel technology is expected to remain the best solution for light-duty and heavy-duty applications, where it offers advantages in terms of both fuel consumption (as well as CO_2 emissions) and fuel costs. Moreover, these advantages may be amplified by means of powertrain electrification.

Low computationally demanding simulation models are generally required for the development of model-based combustion controllers.

Therefore, multidimensional or one-dimensional approaches are currently unsuitable for this purpose. The best candidates for the development of model-based combustion controllers are mean-value zero-dimensional physical models and artificial intelligent systems [8]

Mean-value zero-dimensional models [18-23] are capable of simulating combustion and/or pollutant formation processes on the basis of a physical approach, and at the same time require a much lower computational effort than that required for 3D-CFD or 1D-CFD approaches. These models are usually highly accurate under steady-state operation conditions, and their performance is still acceptable for mildly transient conditions [19]. In general, they do not require a great calibration effort, due to their physics-based nature, and are quite robust outside the calibration range.

Artificial intelligence systems [24-34] include different methodologies, such as the SVM (support vector machine), fuzzy logics and ANNs (artificial neural networks). These methods belong to the black-box category and are often used for model-based control purposes since they require a low computational effort. They are capable of capturing the non-linear behaviors of complex systems,

without the need to model the physics of the system. The main drawback of these types of models is that they in general require a large number of experimental tests for robust training and tend to lose accuracy when extrapolating outside the calibration range. Moreover, they can be subject to overfitting. Among the artificial intelligent systems that are available, ANNs have been shown to play an important role for engine simulation and performance prediction.

Background and contribution of the present study

Given the previous background, a Neural Network-based Real-Time (NNRT) model, which can predict BMEP (Brake Mean Effective Pressure) in diesel engines, was previously developed in [10] for a 1.6L diesel engine. The approach consisted in the use of feed-forward neural networks, which are trained using a large dataset of engine conditions simulated by a mean-value physical combustion model. The resulting ANN-based model had the aim of replicating the outcomes of the mean-value physical model, but with the advantage of requiring a much shorter computational time, in view of its onboard implementation in the engine ECU for cycle-by-cycle BMEP control. Two different versions of the NNRT model were realized in [10], i.e., fuel-to-torque (F2T) and torque-to-fuel (T2F) models. The T2F version can be potentially used as a BMEP controller, since it provides the fuel quantity that has to be injected into the combustion chamber in order to achieve a desired BMEP (or torque) target, which is provided as input.

In this study, the mean-value physical model and the NNRT models have been further developed, starting from the versions developed in [10]. In particular, the following novelties are proposed:

1. Mean-value physical combustion model: an improved version has been developed, assessed and validated for test conditions featuring complex injection patterns, including not only pilot and main pulses, but also multi-after injection shots, under both steady-state and transient conditions. To the best of the authors' knowledge, there is a lack of low-throughput predictive combustion models in the literature that have been validated adopting multi-after injection pulses. It should be noted that the capability of accurately simulating the combustion process when adopting complex injection strategies, including multi-after pulses, is a requirement that has to be satisfied in order to implement a model-based BMEP controller in a commercial engine.
2. F2T and T2F NNRT models: new versions, which include the injection parameters related to the after injection pulses among the inputs, have been developed. The newly developed NNRT models have been trained using a virtual test dataset generated from the improved mean-value physical model, and have been assessed and validated for test conditions featuring multi-after injection shots, under both steady-state and transient conditions. A sensitivity analysis was carried out during the training phase to identify the optimal number of hidden layers and neurons.

The basic idea of the proposed approach is to reduce the calibration effort that is required for engine calibration, especially when several combustion modes and several injection strategies are adopted. In fact, in the traditional map-based approach, several torque-to-fuel ECU maps have to be calibrated (at least one for each combustion mode) at the test bench, and this requires an extensive and costly experimental activity. Instead, a model-based approach for torque control needs a much reduced effort for calibration, since a physical model does not require many experimental tests to be tuned, and the T2F NNRT model is calibrated using the data simulated by the physical model, according to a meta-modeling approach. This can potentially lead to significant cost savings.

Figure 1 shows a flow chart of the proposed methodology.

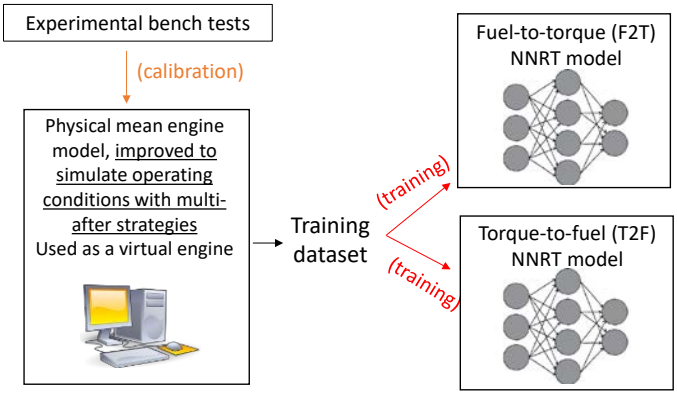

Figure 1. Flow chart of the developed methodology

The paper is organized as follows. First, the engine, experimental setup and the acquired experimental tests are described. Then, the description of the physical combustion model and of the improvements that were adopted in order to make it accurate for the prediction of operating conditions that feature multi-after injection strategies is provided. The description of the NNRT models and of their training procedure is subsequently presented. In the results and discussion section, first, the accuracy of the physical combustion model in terms of heat release and in-cylinder pressure prediction is shown. Then, the performance of the physical combustion model and of the F2T NNRT models, in terms of BMEP prediction, are compared. Finally, the performance of the T2F NNRT model, that can potentially be used as a BMEP controller, is shown.

Engine setup and experimental activity

The experimental tests for the calibration and validation of the models were conducted on a 1.6L Euro 6 GM diesel engine. The main technical specifications of the engine are reported in Table 1. The engine was fueled with standard diesel oil characterized by an average density of 835 kg/m^3 at 14°C, an average viscosity of 2 mm^2/s at 40°C and an average cetane number equal to 43.

Table 1. Main engine specifications.

Engine type	Euro 6 diesel engine
Displacement	1598 cm^3
Bore x stroke	79.7 mm x 80.1 mm
Rod length	135 mm
Compression ratio	16.0
Valves per cylinder	4
Turbocharger	VGT type
Fuel injection system	Common Rail
EGR system	Long route + short route

The engine is equipped with short-route and long-route EGR (Exhaust Gas Recirculation) systems, each of which includes a cooler. A throttle valve is installed upstream from the intake manifold and EGR junction, in order to allow high EGR rates to be obtained

when the pressure drop between the exhaust and intake manifolds is not sufficient.

The test engine was instrumented with piezoresistive pressure transducers and thermocouples to measure the pressure and temperature at different locations, such as upstream and downstream from the compressor, turbine and intercooler, and in the intake manifold. Piezoelectric transducers were installed to measure the pressure time-histories in the combustion chamber of the cylinders. Several consecutive cycles (ranging from 50 to 200) were acquired for each steady-state test, using a crank angle step of 0.1 deg, and the average in-cylinder pressure trace was evaluated and used for model calibration. The in-chamber pressure traces were pegged on the basis of the pressure in the intake manifold, which was measured by means of a high-frequency piezoresistive transducer.

Several tests were conducted under steady-state and transient conditions. Details of the steady-state tests are provided hereafter:

- Full engine maps were carried out for different combustion modes, including or not including multi-after injections strategies, with the engine warmed up. Details about the number and type of combustion modes that are implemented in the ECU, as well as the injection strategies (number of injections and type of injections) which are adopted within each combustion mode, could not be provided for confidentiality reasons of the engine OEM. Therefore, it was only possible to classify the available dataset by splitting it into two sub-datasets, i.e., with and without the use of multi-after strategies. The speed range was between 750 and 3500 rpm, and the BMEP range was between 0 and 23 bar. A total of 521 tests was run.

- Full-factorial sweep tests of the multi-after injection parameters were conducted. Several injection patterns were considered at fixed speed and main injection quantity conditions, several injection patterns were considered, featuring a single after, a double after, a triple after and a quadruple after strategy. The fuel quantity and the SOI of each after pulse was varied (considering 3 levels for each parameter) for each injection pattern, and the other parameters were kept fixed (i.e., fuel quantity of the pilot, main and remaining after pulses, injection timing of the pilot and main pulse and dwell-time of the remaining after pulses). The engine was warmed up. A total of 327 points were considered. The overall engine speed range was between 1000 and 2000 rpm, while the overall BMEP variation was between 2 and 15 bar. Table 2 reports the upper and lower values of the injection timings and quantities for the after pulses.

Table 2. Upper and lower values of the injection timings and quantities for the pilot and after pulses. The angles are indicated in crank angle degrees after top dead center (ATDC)

Type of injection pulse	Min SOI (deg ATDC)	Max SOI (deg ATDC)	Min q_{aft} (mm^3/cyc/cyl)	Max q_{aft} (mm^3/cyc/cyl)
After 1	~10	~60	~1	~9
After 2	~20	~70	~1	~10
After 3	~30	~90	~1	~8
After 4	~50	~80	~1	~9

- Low and negative brake torque tests were run, with the engine warmed up, over a speed range of between 1000 rpm and 4000 rpm, and a BMEP range of between -2.5 and 2.5 bar (72 tests).

- Engine map tests were conducted in combustion modes featuring multi-after injection strategies under cold engine conditions (coolant temperature around 40°C). The speed range was between 1000 and 3750 rpm, and the BMEP range was between 0 and 23 bar. A total of 39 tests were considered.

The overall dataset included a total of 959 steady-state tests.

A list of the transient tests is provided in Table 3.

Table 3. List of the acquired transient tests

Type of transient test	Engine thermal state	Combustion mode (with or w/o multiafter injection strategy)
Time-to-boost ramps	Warm	-w/o (N = 1000, 1500, 2500, 2750, 3250 rpm) -with (N=1000, 1500, 2250, 3250 rpm)
Accelerator pedal position ramps (0-30%, 0-60%, 0-90%)	Warm	-w/o (N = 1000, 1500, 2000, 2500, 3000, 3500 rpm) -with (N = 1000, 1500, 2000, 2500, 3000, 3500 rpm)
Accelerator pedal position ramps (0-30%, 0-60%, 0-90%)	Cold	-w/o (N = 1000, 3000 rpm) -with (N = 1000, 3000 rpm)

Physical and NNRT models

Mean-value physical combustion model

The mean-value physical combustion model was used for the training of the F2T and T2F NNRT models. The model had been developed in previous studies [19]. However, it has been improved and assessed in the present study in order to simulate test conditions featuring complex injection patterns with multi-after strategies. The conceptual scheme of the model is reported in Fig. 2.

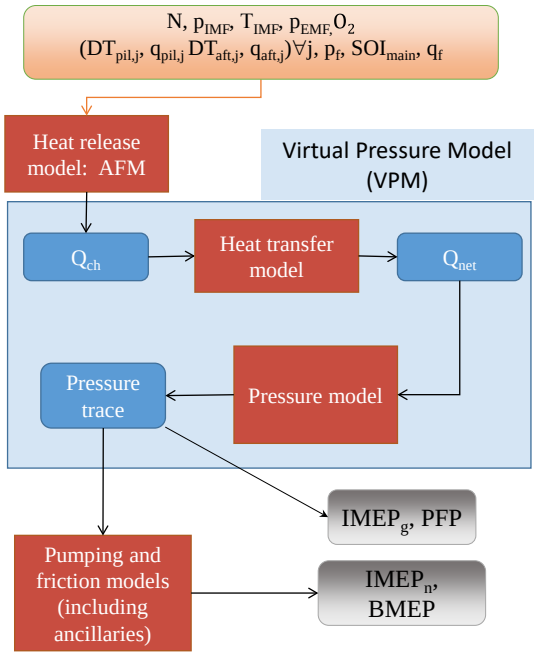

Figure 2. Scheme of the mean-value physical combustion model

The physical model includes the simulation of:

1. Chemical energy release: the simulation is based on the accumulated fuel mass approach (AFM). The input data of the model

are the injection parameters, the main thermodynamic conditions in the intake manifold and the engine operating parameters.

2. In-cylinder pressure: this approach is based on the inversion of a single-zone heat release model that requires the net energy release as input; the latter is derived from the predicted chemical energy release and the heat transfer between the charge and the walls. Polytropic evolutions are assumed during the compression and expansion phases. The simulation of the in-cylinder pressure allows several parameters, such as PFP (peak firing pressure) and $IMEP_g$ (gross indicated mean effective pressure), to be evaluated.

3. Pumping and friction losses: the net IMEP ($IMEP_n$) and BMEP (Brake Mean Effective Pressure) are estimated on the basis of friction (FMEP) and pumping (PMEP) models. The Chen-Flynn approach was used to predict FMEP as a function of the engine speed and PFP.

A detailed description of the model is given in [19]. However, the main equations are synthetically reported in Table 4 (Q_{ch} and Q_{net} models) and in Table 5 (pressure model) to render the paper self-consistent. The model parameters are highlighted in the tables.

Table 4. Main equations of the Q_{ch} and Q_{net} models.

Qch model	$\frac{dQ_{ch,pil,j}}{dt}(t) = \underline{K_{pil,j}}[Q_{fuel,pil,j}(t-\underline{\tau_{pil,j}}) - Q_{ch,pil,j}(t)]$ $\frac{dQ_{ch,main}}{dt}(t) = \underline{K_{1,main}}[Q_{fuel,main}(t-\underline{\tau_{main}}) - Q_{ch,main}(t)] +$ $+\underline{K_{2,main}}\frac{dQ_{fuel,main}(t-\underline{\tau_{main}})}{dt}$ $\frac{dQ_{ch,aft,j}}{dt}(t) = \underline{K_{aft,j}}[Q_{fuel,aft,j}(t-\underline{\tau_{aft,j}}) - Q_{ch,aft,j}(t)]$ $Q_{fuel,j}(t) = \int_{t_{SOI,j}}^{t} \dot{m}_{f,inj}(t) H_L dt \qquad t \le t_{EOI,j}$ $Q_{fuel,j}(t) = \int_{t_{SOI,j}}^{t_{EOI,j}} \dot{m}_{f,inj}(t) H_L dt \qquad t > t_{EOI,j}$ $Q_{ch} = \sum_{j=1}^{n} Q_{ch,j}$ where j indicates the generic injection pulse, H_L indicates the lower heating value of the fuel, K and τ are the combustion rate coefficient and ignition delay coefficient of the Q_{ch} model; pil: pilot pulses, aft: after pulses
Qnet model	$Q_{net,ht} \cong Q_{ch} \frac{m_{f,inj}H_L - \underline{Q_{ht,glob}}}{m_{f,inj}H_L}$ $Q_{net} \cong Q_{net,ht} - \underline{Q_{f,evap}}$ where $Q_{f,evap}$ and $Q_{ht,glob}$ indicate the fuel evaporation heat from SOI to SOC (J) and the heat exchanged between the charge and the walls over the combustion cycle (J), and $m_{f,inj}$ is the total injected fuel mass per cyc/cyl

It should be noted that the chemical energy release model reported in Table 5 has been extended, with respect to previous versions, by adding the contributions of the after pulses.

Table 5. Main equations of the in-cylinder pressure model.

Pressure model	Starting condition (p_{IVC}): $p_{IVC} = p_{IMF} + \underline{\Delta p_{IMF}}$ Compression phase (IVC to SOC): $pV^{\underline{n}} = const$ Combustion phase (SOC to EOC=480°): $p^i = \frac{\Delta Q_{net} - \frac{p^{i-1}}{2}(V^i - V^{i-1}) + \frac{1}{\gamma-1}p^{i-1}V^{i-1}}{\frac{V^i - V^{i-1}}{2} + \frac{V^i}{\gamma-1}}$ Expansion phase (EOC to EVO): $pV^{\underline{n'}} = const$ where p_{IMF} indicates the intake manifold pressure, p_{IVC} the in-cylinder pressure at IVC, and n and n' the compression and expansion polytropic exponents.
Estimation of IMEP and BMEP	$IMEP_g = \frac{\int_0^{360} pdV}{V_0}$ $IMEP_n = IMEP_g - \underline{PMEP}$ $BMEP = IMEP_n - \underline{FMEP}$

The pressure discretization scheme shown in Table 5 was proposed in [8]. In that study, it was shown that such a scheme allows the loss in accuracy to be reduced to a great extent when the computational step is increased from 0.1 to 1 deg.

The isentropic coefficient $\gamma = c_p/c_v$ was set constant and equal to 1.37.

Model calibration

The model calibration phase is performed in two steps:

- Step 1: this is constituted by the identification of the optimal values for the model tuning coefficients highlighted in Table 4 and Table 5, for each available experimental test. Basically, it is a test-by-test calibration of the parameters.
  The calibration parameters of the Q_{ch} model are tuned as follows. First, the start of combustion (SOC) is identified for each pulse, by analyzing the experimental heat release trace (which is derived from the measured in-cylinder pressure). This allows the ignition delay parameters (τ) to be derived, as the difference between the SOI and SOC angles of each pulse. Subsequently, the K parameters are identified, in order to achieve the best possible matching between the predicted and experimental Q_{ch} profiles, using a least square fitting algorithm. The experimental values of the $Q_{f,evap}$ and $Q_{ht,glob}$ parameters of the Q_{net} model are then derived, for each calibration point, on the basis of the pressure-derived net energy release. The experimental values of the Δp_{IMF}, n and n' parameters of the pressure model are derived, for each calibration point, on the basis of the analysis of the measured in-cylinder pressure trace. Finally, the experimental values of PMEP are obtained from the analysis of the pressure curve during the gas exchange process, while FMEP is obtained as the difference between the pressure-derived $IMEP_n$ and the measured BMEP.
- Step 2: this consists in the identification of physically consistent correlations for each model parameter, as a function of significant engine variables, using the optimal values identified, test by test, in step 1. The input variables are selected by making a trade-off between prediction accuracy (which takes benefit of a large number of input variables) and model robustness (which suffers from the adoption of a large number of variables).

Several modifications were made, in comparison with the baseline procedure developed in previous studies, in order to improve the calibration of the model when multi-after injections are used:

- The calibration phase of the 'K' coefficients of the Q_{ch} model was assessed by considering the combustion of each injection pulse separately. This means that, in order to calibrate, for example, the 'K' coefficient of the 'after 2' pulse (i.e., $K_{aft,2}$), the part of heat release used for least square minimization is that included between the SOC of the 'after 2' pulse and the SOC of the 'after 3' pulse. This is illustrated in Fig. 3. The main reason for the small discrepancy between the predicted and experimental trends of Q_{ch} in correspondence to the combustion of the last after pulse, in Fig. 3, could be due to uncertainties in the injection quantities that are used in the model, which were derived from the ECU setpoints.

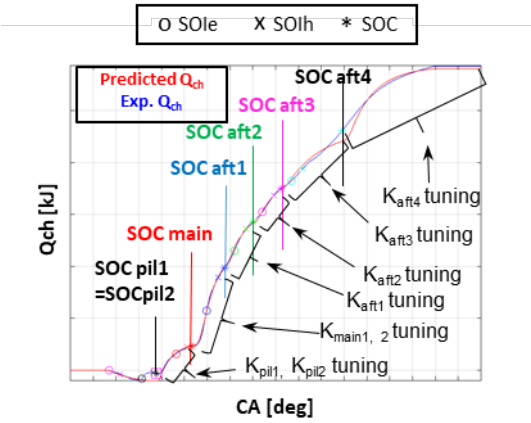

Figure 3. The heat release intervals considered for the calibration of each K parameter of the Q_{ch} model. SOIe: electric SOI; SOIh: hydraulic SOI.

- The Q_{ch} model calibration was performed through an automatic tool in order to save time. In particular, the tool first calculates the value of the start of combustion of each pulse by analyzing the peaks of the experimental heat release rate (using the "findpeak" function of matlab), and evaluates the ignition delay values (τ) for each injection pulse, as the difference between the start of combustion and the hydraulic start of injection. Once the τ values are known, the tool applies the heat release model equations and tunes the K values of each injection pulse by means of least square minimization, in order to have the best matching with the experimental heat release trace. As previously stated, the K value of each pulse is calibrated independently, on the relevant heat release interval between its SOC and the SOC of the following pulse. However, the tool may fail to correctly identify the correct calibration parameters for some operating conditions. The main reasons for this are a possible erroneous SOC identification of the different pulses, and discrepancies between the actual injected fuel quantity and the desired setpoint one, which is derived from the injector maps and used in the model. These discrepancies can lead to a poor matching between the predicted and experimental heat release curves, and therefore to the identification of erroneous values of the K parameters (especially for the main pulse). Therefore, these points should be excluded when the correlations for the K and τ parameters are built in calibration step 2. The point exclusion criteria are reported in Table 6.

Table 6. Criteria for point exclusion during the Q_{ch} model calibration phase

Type of parameter	Criteria that have to be satisfied for acceptance of the calibration point in the dataset used for the building of the correlations
K_{main}	Injection strategy w/o multiafter, τ_{main} <15 deg
τ_{main}	Injection strategy w/o multiafter
$K_{aft,1,2}$	$0<K_{aft,1,2}<0.2deg^{-1}$&$0<\tau_{aft,1,2}<15deg$
$K_{aft,3,4}$	$0<K_{aft,3,4}<0.2deg^{-1}$&$0<\tau_{aft,3,4}<25deg$
$\tau_{aft,1,2}$	$\tau_{aft,1,2}<15deg$
$\tau_{aft,3,4}$	$\tau_{aft,3,4}<25deg$

- Finally, it was verified that when multi-after injection strategies are adopted, a significant error occurs, especially at lower loads, if a single correlation is identified for the heat transfer when the whole test dataset is considered (with and w/o multi-after). However, an improvement , which involves splitting the heat transfer calibration dataset into four parts (high load without multi-after strategy, low load without multi-after strategy, high load with multi-after strategy, low load with multi-after strategy), and then identifying four separate exponential formulas, was made.

The identified correlations of the Q_{ch} and Q_{net} model calibration parameters are reported hereafter:

$$K_{pil}[\frac{1}{\deg}] = 5.04E-09 * e^{\frac{-5.28E03}{T_{SOC,pil}}} O_2^{8.719} N^{-0.551} q_{f,pil}^{-0.373} q_f^{0.625.} \quad (1)$$

$$K_{1,main}[\frac{1}{\deg}] = 0.011 p_f^{-0.207} \rho_{SOC_{main}}^{0.2185} N^{0.438.} q_f^{-0.255} \quad (2)$$

$$K_{2,main}[-] = 17.9 p_f^{0.756} \rho_{SOCmain}^{1.018} N^{-1.596} q_f^{-0.284} \quad (3)$$

$$K_{aft,1}[\frac{1}{\deg}] = 0.78 p_f^{0.626} q_{main}^{-0.201} N^{-0.004} q_{aft,1}^{0.123} SOI_{aft,1}^{-1.023} \quad (4)$$

$$K_{aft,2}[\frac{1}{\deg}] = 30.658 p_f^{0.467} O_2^{-1.463} N^{-0.519} q_f^{-0.175} \quad (5)$$

$$K_{aft,3}[\frac{1}{\deg}] = 0.269 p_f^{-0.416} O_2^{-0.533} N^{0.285.} q_f^{0.335} \quad (6)$$

$$K_{aft,4}[\frac{1}{\deg}] = 4.184E-8 p_f^{-0.630} O_2^{4.323} N^{0.455.} q_f^{0.680} \quad (7)$$

$$\tau_{pil}[\deg] = 310.54 \rho_{SOI,pil}^{-0.84} \cdot e^{\frac{1.06E3}{T_{SOI,pil}}} \cdot O_2^{0.92} \quad (8)$$

$$\tau_{main}[\deg] = 1.35 p_f^{-0.45} \rho_{SOI,pil}^{-1.44} O_2^{-0.45} N^{1.20} q_f^{-0.03} \quad (9)$$

$$\tau_{aft,1}[\deg] = 6.69E-11 \cdot p_f^{-0.713} q_{main}^{-0.075} N^{1.354} q_{aft,1}^{0.190} SOI_{aft,1}^{3.16} \quad (10)$$

$$\tau_{aft,2}[\deg] = 8.02E-11 p_f^{-0.285} O_2^{-1.814} N^{1.213} q_f^{-0.268} SOI_{aft,2}^{3.912} \quad (11)$$

$$\tau_{aft,3}[\text{deg}] = 8.60E-13\, p_f^{-0.470} O_2^{-2.193} N^{1.147} q_f^{-0.466} SOI_{aft,3}^{5.28} \quad (12)$$

$$\tau_{aft,4}[\text{deg}] = 3.59E4\, p_f^{-0.618} O_2^{-0.271} N^{0.980} q_f^{0.055} SOI_{aft,2}^{-1.848} \quad (13)$$

$$Q_{f,evap}[kJ] = 3.58E\text{-}12\, T_{IMF}^{3.306} N^{0.417} q_f^{0.018} \quad (14)$$

$$Q_{ht,glob}[kJ] = 4.70E-3 \cdot p_f^{0.392} p_{IMF}^{-0.220} O_2^{0.74} N^{-0.497} q_f^{0.868} \quad (q \le 20mm^3, w/o\ multi-after\ strategy) \quad 15)$$

$$Q_{ht,glob}[kJ] = 6.79E-4 \cdot p_f^{-1.767} p_{IMF}^{-0.258} O_2^{1.007} N^{1.537} q_f^{0.872} \quad (q \le 20mm^3, with\ multi-after\ strategy) \quad 16)$$

$$Q_{ht,glob}[kJ] = 0.012 \cdot p_f^{-0.017} p_{IMF}^{-0.514} O_2^{-0.135} N^{-0.268} q_f^{1.418} \quad (q > 20mm^3, w/o\ multi-after\ strategy) \quad 17)$$

$$Q_{ht,glob}[kJ] = 1.66E2 \cdot p_f^{-0.169} p_{IMF}^{-0.779} O_2^{-3.694} N^{0.164} q_f^{1.454} \quad (q > 20mm^3, with\ multi-after\ strategy) \quad (18)$$

where ρ_{SOI}, ρ_{SOC} in equations (1-18) indicate the in-chamber densities evaluated at the start of injection and combustion, respectively, and are expressed in kg/m^3. The injection pressure p_f is expressed in bar, the engine speed N in rpm, the total injected fuel quantity q_f (used as a load parameter) in mm^3/cyc/cyl and the intake oxygen concentration O_2 in %. T_{IMF} and p_{IMF} indicate the intake manifold temperature and pressure, respectively.

It should be noted that the units of the K and τ parameters are expressed as a function of the crank angle. This is because the heat release model equations reported in Table 5 are implemented over a crank angle domain.

The following correlations, which are functions of the intake manifold thermodynamic conditions and of the engine load and speed, were identified for the pressure model parameters:

$$n = 1.34 T_{IMF}^{-0.0203} N^{0.0126} q_f^{0.006} \quad (19)$$

$$n' = 0.050 \cdot T_{IMF}^{0.564} N^{-0.0004} q_f^{-0.005} \quad (20)$$

$$\Delta p_{IMF}[bar] = 0.035\, p_{IMF}^{0.980} N^{0.167} q_f^{-0.005} \quad (21)$$

The following correlation was identified to evaluate the PMEP of the engine considered in this study:

$$PMEP[bar] = 0.0054 \cdot p_{EMF}^{0.939} N^{0.387} - 0.077 \cdot p_{IMF}^{0.910} N^{0.331} \quad (22)$$

The Chen-Flynn approach [35] was adopted to estimate FMEP, and the following correlation was identified for the engine considered in this study:

$$FMEP[bar] = 0.040 + 1.883E-4 \cdot N + 6.245E-8 \cdot N^2 + 0.002 \cdot PFP \quad 23)$$

where the engine speed is expressed in rpm and PFP is expressed in bars. The squared correlation coefficient R^2 between the predicted and experimental values of FMEP is of the order of 0.74.

NNRT models

The neural network-based real-time (NNRT) developed in this study models are constituted by feed-forward, single hidden layer ANNs, which have been trained using data simulated by the physical mean-value combustion model, according to a meta-modeling approach.

Feed-forward ANNs were chosen, since it was verified that they are sufficiently accurate for the required application, and moreover because they are typically adopted in the literature for similar applications [10]. Concerning the choice of the feed-forward NNs, we made a sensitivity analysis also concerning the number of inner layers and the number of neurons, and we verified that a network with single inner layer allows to reproduce very well the physical model behaviour, therefore it was not necessary to adopt a larger number of inner layers or a more complex neural network structure.

As previously stated, two different versions of the NNRT model were realized, i.e., the F2T and T2F models. The T2F version can potentially be used as a BMEP controller, since it provides the fuel quantity of the main pulse (or the total fuel quantity) that has to be injected into the combustion chamber in order to achieve a desired BMEP (or torque) target, which is provided as input.

The NNRT model training data were derived by resorting to a local DoE approach (see [10]), applying a latin hypercube technique around each point of each available engine map (i.e., for several combustion modes). The following quantities were varied around their nominal values: injection pressure (p_f), intake O_2 concentration (O_2), intake and exhaust manifold pressure (p_{IMF}, p_{EMF}), intake manifold temperature (T_{IMF}), dwell-angle (DA) and injected fuel quantity of 4 after pulses and 2 pilot pulses, and start of main injection (SOI_{main}). The same variables were used as inputs for the NNRT models (except for the dwell-angle of the injection pulses, which was replaced by the start of injection), as shown in Fig.4, together with the q_{main} parameter (for the F2T NNRT model) and the BMEP target (for the T2F NNRT model).

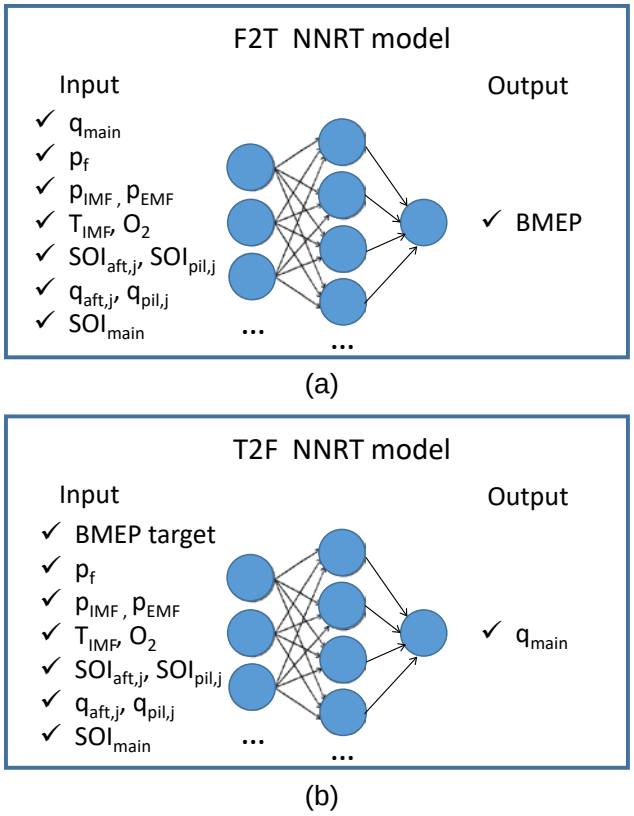

Figure 4. Schemes of the F2T and T2F NNRT models.

It should be noted that the T2F model can provideeither the main injection quantity (q_{main}) or the total injected quantity (q_f) as output, depending on the specific requests of the ECU in which it is integrated.

The variation range of each parameter of the DoE is reported in Table 7.

Table 7. Variation range of each parameter of the DoE

Parameter	Variation range	Absolute (A) or relative (R)
p_f	±20%	R
O_2	±2%	A
p_{IMF}, p_{EMF}	±20%	R
T_{IMF}	±20°	A
$DA_{aft,j}$, $DA_{pil,j}$	±60%	R
SOI_{main}	±5 CA deg	A
$q_{aft,j}$, $q_{pil,j}$	±30%	R

Two separate datasets were generated for the training of the NNRT models. In the first one,100 points were generated for each local DoE in all the combustion modes and 400 points were generated in the second one. The overall size of the two datasets is of the order of 50000 (50k) and 200000 (200k) points, respectively.

The same datasets were used for the training of the F2T and T2F models.

Calibration procedure

The calibration procedure was carried out in Matlab R2016b, by conducting a sensitivity analysis, in which the number of inner layers (1, 2), the number of neurons of each inner layer (1, 2, 4, …, 20) and the calibration datasets (50k, 200k points) were varied, as shown in Table 8. This training schedule led to the evaluation of 40 different types of NN structures. The neural network training was performed using the standard Levemberg-Marquardt method and selecting 50% of the data for calibration, 25% for validation and 25% for testing.

Table 8. Cases investigated for the training of the T2F and F2T NNRT models.

	Training dataset size: 50k points	Training dataset size: 200k points
1 hidden layer	Number of neurons of each hidden layer: 1, 2, 4, 6, …, 20	Number of neurons of each hidden layer: 1, 2, 4, 6, …, 20
2 hidden layers	Number of neurons of each hidden layer: 1, 2, 4, 6, …, 20	Number of neurons of each hidden layer: 1, 2, 4, 6, …, 20

The number of neurons was not increased beyond 20, because it was noted that, in general, the predictive performance and the robustness of the trained neural network tended to reduce when a too large number of neurons was used for constant calibration datasets. The number of hidden layers was not increased beyond 2, because it was noted that the neural network featuring two hidden layers showed a more irregular behavior than that featuring a single hidden layer (i.e., low errors for several points, and extremely high errors for a few points), without any advantage in terms of predictive capability. In fact, the neural network featuring a single inner layer already provided very similar results to those of the physical model. Moreover, an increase in the virtual calibration dataset would be required if the number of hidden layers were increased, and this would consequently increase the training time without introducing any benefits to the network performance.

Since it was noted that the performance of the network, for a given structure, in terms of number of layers and neurons, changed significantly as the initial conditions for training were changed, 15 training attempts were made for each investigated structure by randomly changing the initial conditions, and the attempt which led to the best predictive performance was then taken.

The predictive capability of each neural network structure was evaluated after the training phase by applying each network to the experimental dataset (not used for training), and to the overall virtual dataset used in the training procedure (including calibration, validation and testing points). The corresponding root mean square errors (indicated as $RMSE_{val}$ and $RMSE_{tr}$, respectively) were then estimated by comparing the predicted and experimental values of BMEP values (for the F2T NNRT model) and q_f (for the T2F NNRT model). It should be noted that $RMSE_{val}$ is the real indicator of the predictive capability of the neural network, while the $RMSE_{tr}$ parameter only measures the capability of the network to fit the dataset used for training.

The s best neural network structure was chosen by making a trade-off between the accuracy and the neuron number. Fig. 5a shows the accuracy of the F2T NNRT model with 1 hidden layer calibrated

using the 200k dataset, as an example, in terms of $RMSE_{val}$ and $RMSE_{tr}$ as a function of the neuron number.

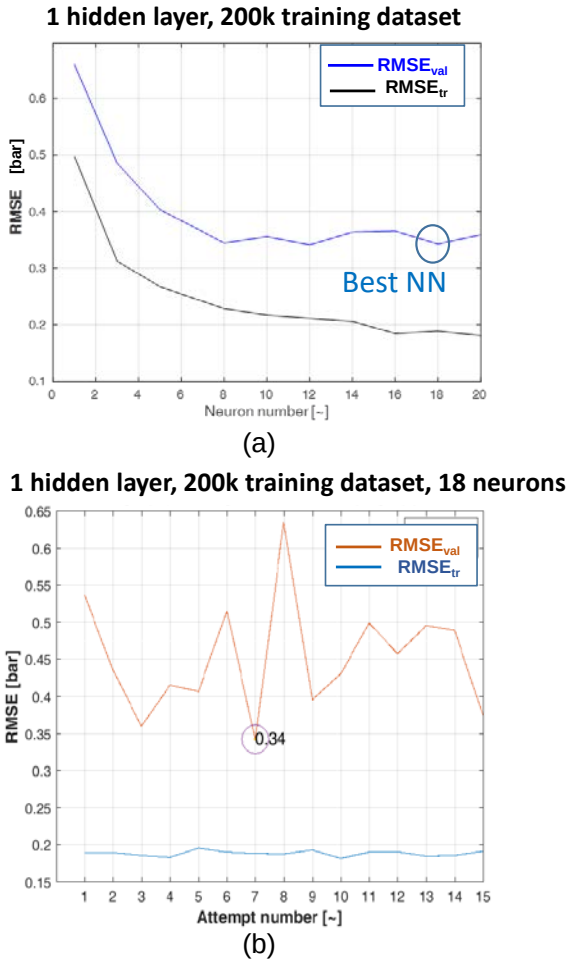

Figure 5. (a): $RMSE_{val}$ and $RMSE_{tr}$ values as functions of the number of neurons of the hidden layer, for the F2T NNRT model with 1 hidden layer, calibrated over the 200k dataset. (b): $RMSE_{val}$ and $RMSE_{tr}$ values for the 15 different training attempts of the network featuring 18 neurons, varying the initial conditions.

It can be seen that, in general, the $RMSE_{tr}$ always tends to decrease when the neuron number increases, while $RMSE_{val}$ tends to stabilize or even increase when the number of neurons of the hidden layer increases, and this behavior is likely to indicate overfitting. Finally, 18 neurons were selected as the best trade-off between predictive accuracy and neuron number. Fig. 5b shows how $RMSE_{val}$ and $RMSE_{tr}$ changed for 15 different training attempts, when varying the initial conditions. The 7^{th} attempt was selected as it leads to the minimum $RMSE_{val}$value.

The optimal neural network structure was also selected by evaluating the robustness of the network. This was done by checking that the network did not feature any highly oscillating errors, in terms of BMEP or fuel estimation, such as particularly low errors in several points and very large errors in a few points, since such behaviour is undesirable for real time control applications. It was verified that this behaviour is more likely to occur when adopting two hidden layers.

The optimal structures selected for the T2F and F2T NNRT models are reported in Table 9.

Table 9. Optimal structures selected for the T2F and F2T NNRT models, along with the $RMSE_{val}$ values of BMEP (F2T model) and q_f (T2F model).

	Training dataset size:	Number of hidden layers	Number of neurons of the hidden layer	$RMSE_{val}$
F2T NNRT model	200k points	1	18	0.35 bar
T2F NNRT model	200k points	1	12	1.17 mm3/cyc/cyl

Although the RMSE for the validation phase is basically constant for a neuron number higher than 8, we finally decided to choose the net with 18 neurons since the RMSE for the training phase is lower.

Finally, it was also interesting to verify the computational time that was required for the generation of the DoE and for the training of the neural networks, as a function of the neuron number, the number of hidden layers and the number of calibration points. Basically, the mean-value physical model requires an average computational time of about 9 minutes for the generation of the 50k virtual dataset, and of 33 minutes for the generation of the 200k dataset, when it is run, in Matlab R2016b, on a 3.4 GHz PC equipped with 32 GB of RAM.

The results related to the computational time required for training are shown, in Fig. 6, for the different investigated F2T NNRT models (similar results were verified for the T2F NNRT model). The figure reports the computational time (h) that is required for the training of the F2T NNRT model, as a function of the total number of neurons of the hidden layers, for different training datasets (50k, 200k, indicated with 'S50' and 'S200', respectively) and different numbers of hidden layers (1, 2, indicated with 'L1' and 'L2', respectively).

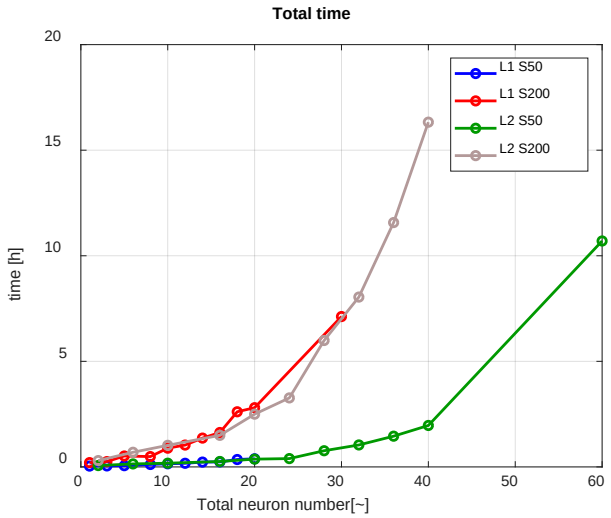

Figure 6. Computational time (h) required for the training of the F2T NNRT model, as a function of the total number of neurons of the hidden layers, for different training datasets (50k, 200k, indicated with 'S50' and 'S200', respectively) and the different numbers of hidden layers (1, 2, indicated with 'L1' and 'L2', respectively).

It can be seen, in Fig.6, that the computational time is closely related to the total number of neurons of the hidden layers, regardless of the number of hidden layers of the neural network.

The selected neural network for the F2T NNRT model (L1 S200, with 18 neurons in the hidden layer) requires a training time of the order of 3h.

Results and discussion

The main results that are reported in this section can be summarized as follows. First, the capability of the mean-value physical combustion model to estimate the heat release, heat release rate and in-cylinder pressure, when adopting complex injection strategies, is discussed for two selected engine conditions.

A comparison of the performance of the mean-value physical combustion model and of the F2T NNRT model, in terms of BMEP estimation under steady-state and transient operation, is then reported.

The performance of the T2F NNRT model is then discussed under steady-state and transient operation.

Finally, a comparison between the computational time required for the physical model and that required by the LNN model is reported.

It should be noted that, when the models are applied under steady-state operation conditions, all the inputs, except for the intake pressure and temperature, were taken from bench measurements (i.e., exhaust pressure, intake O_2 concentration, injected fuel quantity…). Instead some inputs were not available from the test bench for the transient validation, i.e., injected fuel quantity and exhaust manifold pressure. These quantities were obtained from ECU maps or models.

Mean-value physical combustion model: estimation of the heat release, heat release rate and in-cylinder pressure

The capability of the mean-value physical combustion model to estimate the heat release, the net heat release rate and the in-cylinder pressure, when complex injection patterns featuring multi-after injections are adopted, has been evaluated. It should be noted that the model was applied to all the available 959 steady-state tests (see the next sections). However, for the sake of brevity, only two engine points of the full-factorial sweep tests have here been selected, one to be representative of a low-load engine condition (N=1250rpmxBMEP=3.4bar), and the other one of a medium-high load condition (N=2000rpmxBMEP=11.6bar). The selected engine points feature 3 and 4 after pulses, respectively. The results are shown in Fig. 7 (low load point) and Fig. 8 (medium-high load point). A comparison of the predicted (red) and experimental (blue) trends of the cumulative chemical heat release (a), of the net heat release rate (b) and of the in-cylinder pressure (c) are shown in each figure. For confidentiality reasons, the chemical energy release and net heat release rate curves were normalized with respect to a fixed value, and only relative variations are shown for the pressure and crank angle values. Moreover, the SOIe, SOIh and SOC values are also indicated in the heat release and net heat release rate charts with circle, cross and star symbols, respectively. The injection rate profiles are also plotted.

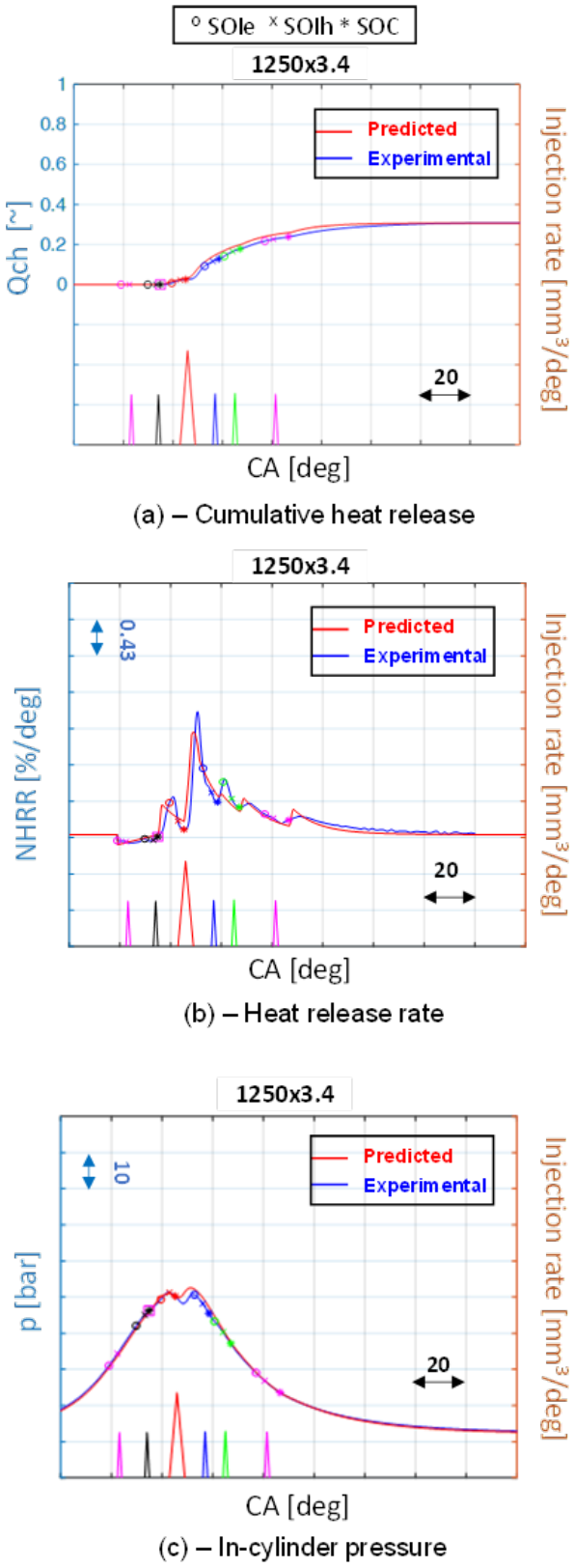

Figure 7. Comparison of the predicted (red) and experimental (blue) trends of Q_{ch} (a), net heat release rate (b) and in-cylinder pressure (c) for a low load point of the full-factorial sweep tests related to the multi-after parameters.

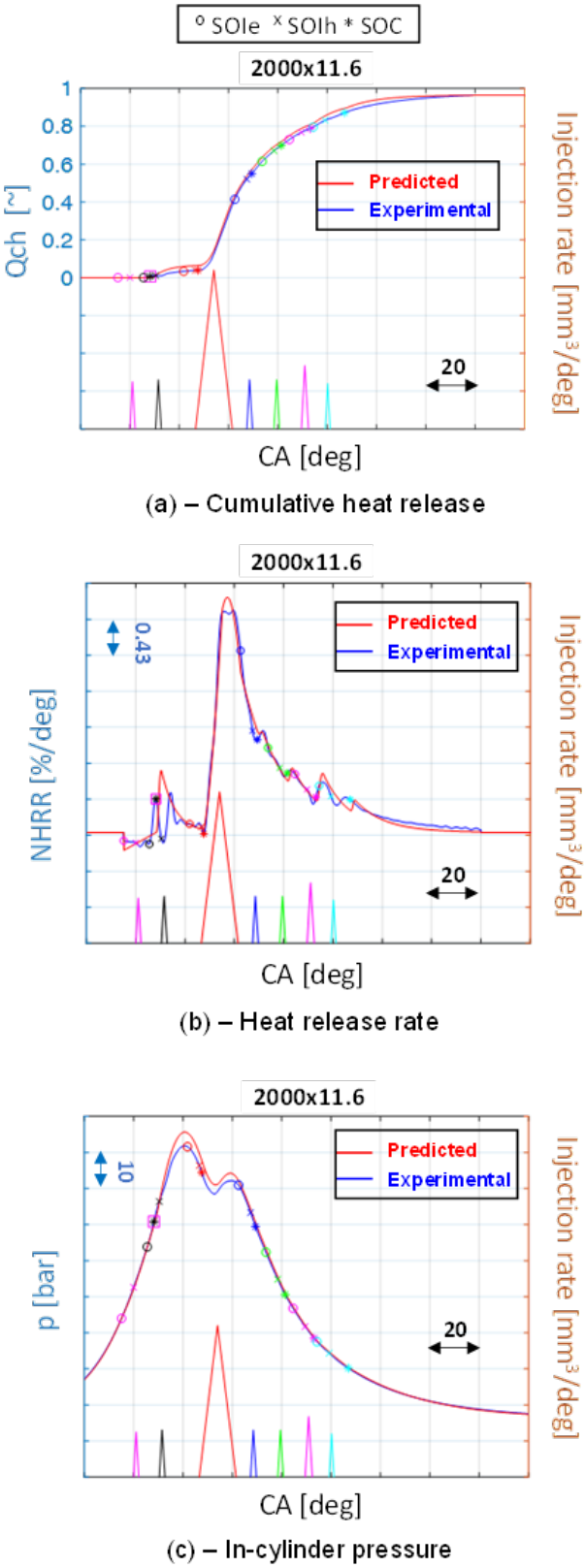

Figure 8. Comparison of the predicted (red) and experimental (blue) trends of Q_{ch} (a), net heat release rate (b) and in-cylinder pressure (c) for a medium-high load point of the full-factorial sweep tests related to the multi-after parameters.

It can be seen that the mean-value physical model is able to reproduce the complex trends of the chemical heat release, heat release rate and in-cylinder pressure for the considered examples when complex injection strategies are adopted. The main reason for the small discrepancies between the predicted and experimental trends of NHRR in Figs. 7-8 could be due to uncertainties in the injection quantities that are used in the model, as well as to a non-optimal estimation of the 'K' parameters of the heat release model, which are derived from the correlations (1-7). However, these local errors in heat release prediction do not affect significantly the accuracy in torque prediction, as will be shown in the next sections.

Comparison of the performance of the physical and F2T NNRT models

The physical and F2T NNRT models have been applied to the steady state test dataset. Figure 9 reports the predicted vs. experimental values of BMEP, obtained using the two models. The different types of tests are highlighted in the charts with different colors ('w/o' or 'w' denote the conditions without or with the multi-after strategy, 'Map' denotes the engine map tests, 'FF' denotes the full-factorial sweep tests of the multi-after injection parameters, 'Neg' the low and negative torque tests, and 'Map Cold' represents the engine map tests with multi-after in cold conditions). The prediction accuracy of each model was quantified by means of the RMSE. Moreover, an error boundary, which corresponds to 0.39 bar when the BMEP values are lower than 3.93 bar, and to 10% when the BMEP values are higher or equal to 3.93 bar was defined, and the percentage of points for which the absolute error is lower than the defined boundary (indicated with P) was estimated.. A comparison of the RMSE and P values of the physical and the F2T NNRT models is reported in Fig. 9 for the different test types.

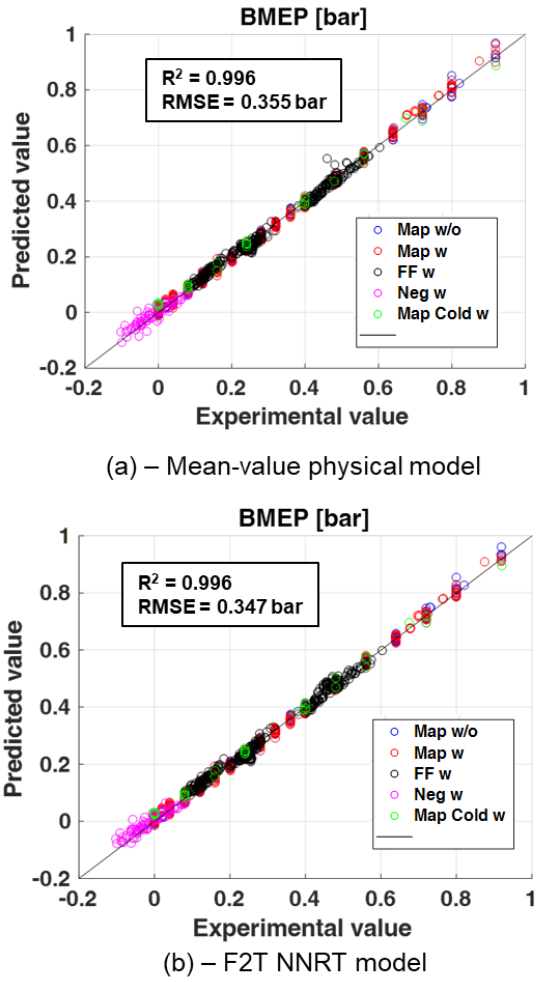

Figure 9. Predicted vs. experimental BMEP values for the steady-state test dataset, considering the mean-value physical combustion model (a) and the F2T NNRT model (b).

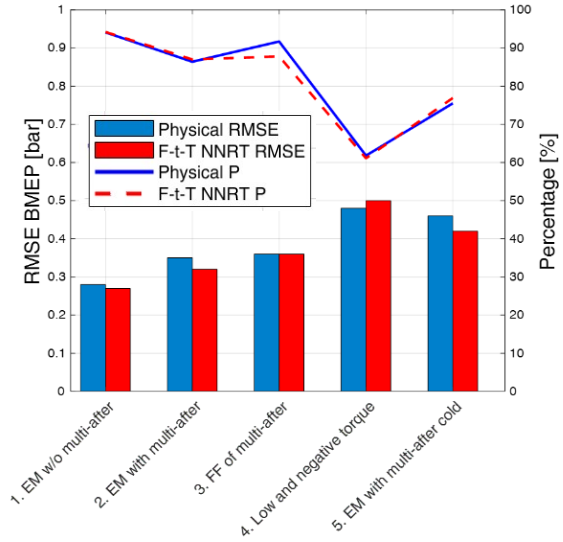

Figure 10. Comparison of the RMSE and P values of the physical and the F2T NNRT models, with reference to BMEP estimation, for the different steady-state tests.

It can be seen, from Figures 9-10, that the F2T NNRT model features a similar accuracy to that of the mean-value physical model (the overall RMSE is of the order of 0.35 bar). Moreover, the results reported in Figure 10 indicate that the accuracy of the models does not deteriorate significantly when multi-after injection strategies are adopted (e.g., the RMSE is of the order of 0.27-0.28 bar for the engine map tests w/o multi-after pulses, and of the order of 0.32-0.35 bar for the engine map tests with multi-after pulses). The error also remains low for the low and negative torque tests (RMSE 0 0.48-0.50 bar) and for engine map tests under cold conditions with multi-after strategies (RMSE = 0.42-0.46 bar). The results obtained under cold engine conditions indicate that engine brake torque is not affected to any great extent when the coolant temperature is higher than 40°C. In general, it can also be seen that around 90% of the points are within the error boundary for the first three test categories, while the percentage is minimum for the low/negative torque tests. However, the torque prediction for these test cases is affected by a high relative error, since the absolute values of BMEP are very low.

The performance of the two models was also investigated under transient operation conditions. Figure 11 shows the comparison between the values of RMSE and P, concerning the BMEP estimation, for the mean-value physical combustion model and F2T NNRT model, for the different considered tests.

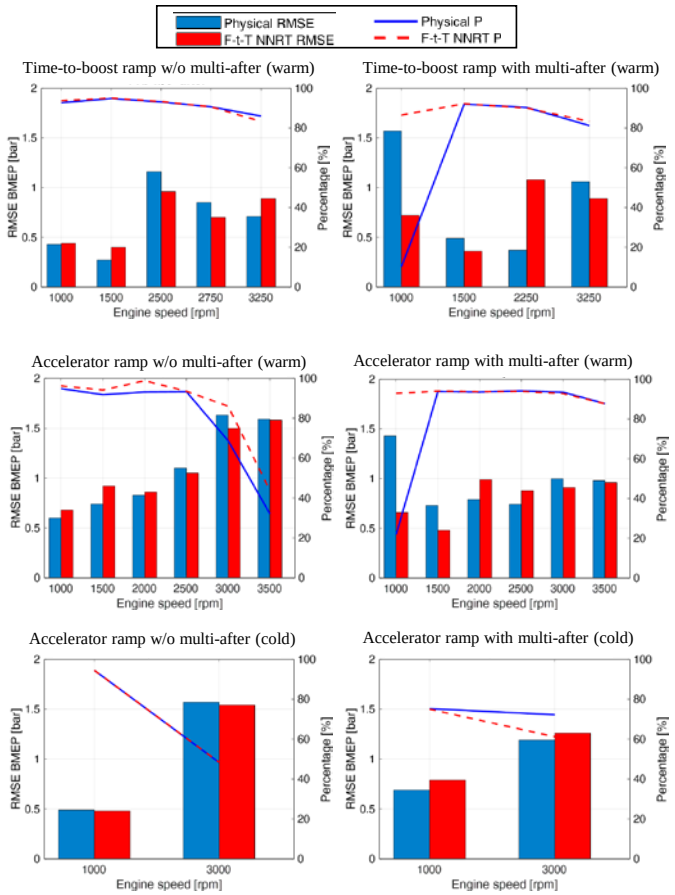

Figure 11. Comparison of the RMSE and P values of the physical and the F2T NNRT models, with reference to BMEP estimation, over the different transient tests.

It can be seen that, in general, although the accuracy of the estimation of BMEP may change significantly, depending on the specific test, it is not deteriorated by the adoption of combustion modes featuring multi-after injection strategies. Moreover, it should be noted that, in general, the error is higher than that of the steady-state tests. This error may also be due to reasons other than the model accuracy. For example, it may be affected by temporal shift errors between some input quantities of the model and the measured BMEP trace. It was in fact verified that short temporal shifts may

lead to a large increase in the RMSE values. In addition, inaccurate estimations of intake O_2 and exhaust manifold pressure may also contribute to these increases. Finally, it should be noted that the fuel mass provided to the models as input was taken from the injector maps of the ECU for the transient tests, since the measurement of the bench flow meter was affected by excessive noise under transient operation conditions. This may have led to an increase in the RMSE error, as will be shown in the next paragraphs.

Two of the previous transient tests are shown in Figures 12-13 as examples. The figures report a comparison of the predicted (blue line: mean-value physical model, dashed black line: F2T NNRT model) and experimental (red line) trends of BMEP over two transient tests featuring combustion modes without (a) and with (b) multi-after injection strategies. Only relative variations of BMEP are shown in the charts, for confidentiality reasons. Figure 12 refers to a time-to-boost ramp at N=1500 rpm, while Fig. 13 refers to an accelerator pedal position ramp at N=3500 rpm. These two transient tests were selected in order to show why the percentage of points within the error boundary may be low for some cases (i.e., accelerator pedal position ramp without a multi-after strategy). The upper and lower boundaries of BMEP, which were defined in order to estimate the 'P' parameter in Fig. 11, are also reported in the figures with dashed red lines.

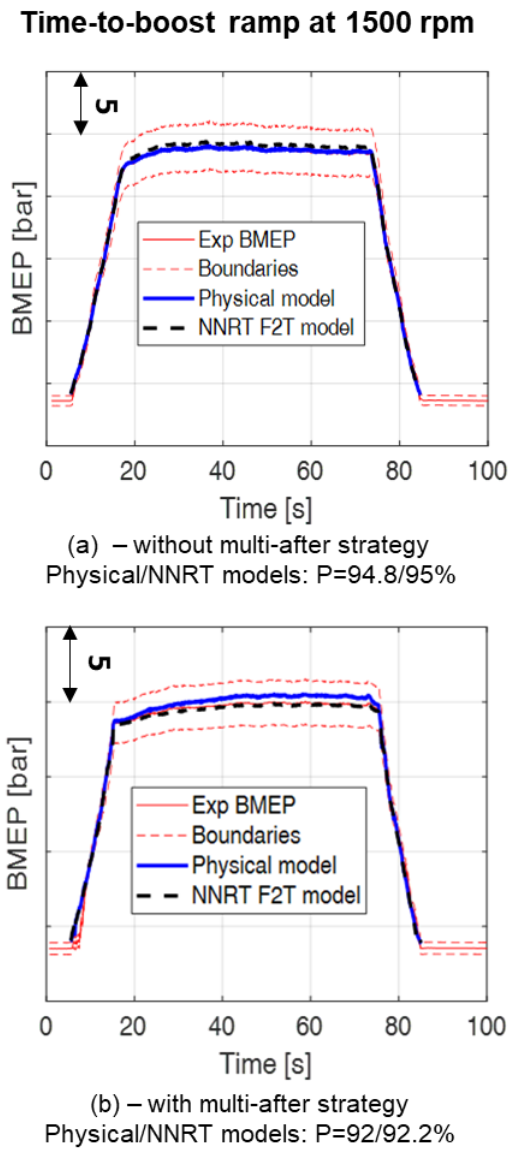

Figure 12. Experimental and predicted trends of BMEP over the time-to-boost ramp at N=1500 rpm for test cases featuring combustion modes without (a) and with (b) multi-after injection strategies

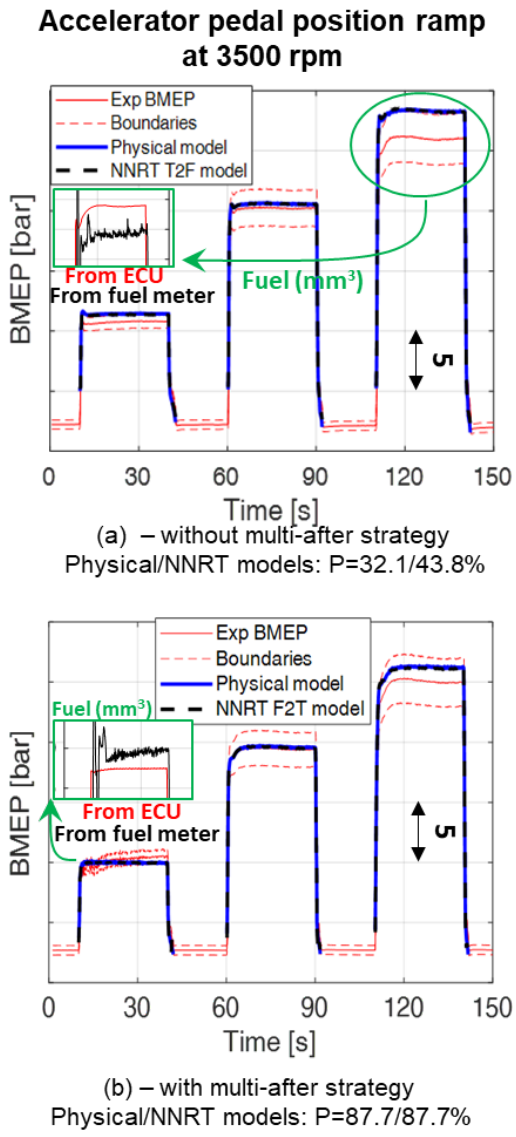

Figure 13. Experimental and predicted trends of BMEP over an accelerator pedal position ramp at N=3500 rpm for test cases featuring combustion modes without (a) and with (b) multi-after injection strategies.

The figures show that the results of the F2T NNRT model are in line with those of the physical model also in transient operation conditions. It can be seen, in Fig. 13a, that, although the percentage of points within the error boundary is 32.1%, the predicted BMEP values are in line with the upper boundary. Moreover, the BMEP error may not only be due to the accuracy of the model, but also to the fact that the setpoint fuel quantity derived from the ECU maps (which is provided to the models as input) may be different from the real injected quantity. Figures 13a and 13b in fact show a comparison between the fuel quantity measured from the fuel meter (black line in the small box) and the ECU fuel setpoint (red line in the small box). It can be seen that the ECU setpoint quantity is higher than the real injected quantity for the test without a multi-after strategy, and lower for the test with a multi-after strategy. The BMEP error is in line with the fuel error in both cases. It was not possible to use the fuel quantity from the test bench fuel meter as input for the model over the transients, due to high oscillations and to a slow dynamic response.

It is also interesting to note, in Fig. 13b, that a slightly increasing trend in the real injection quantity occurs, even though the fuel quantity setpoint of the ECU is constant. This may be related to dynamic effects, such as pressure waves in the injection pipes or thermal effects on the injectors, which may lead to different injected quantities, even for constant injection pressure and energizing time values. Finally, Fig. 14 shows a zoomed view of the rising and descending edges of the transient tests shown in Figs. 12-13. With reference to the accelerator pedal position ramp test, the central ramp was considered.

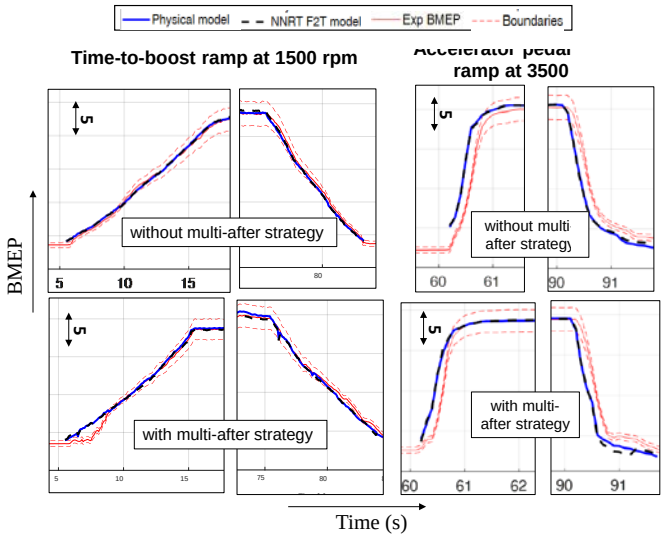

Figure 14. Zoomed view of the rising and descending edges of the transient tests shown in Figs. 12-13.

Performance of the T2F NNRT model

The performance of the T2F NNRT model is discussed in this section.

Figure 15 reports the predicted vs. experimental values of the total injected quantity q_f. The fuel quantity values were normalized for confidentiality reasons. The different types of tests are highlighted in the charts with different colors. The prediction accuracy of each model is quantified by the squared correlation coefficient (R^2) and by the RMSE. Moreover, a fuel error boundary, which was derived from the BMEP error boundary, was defined considering an average value of the engine thermal efficiency, and the percentage of the points for which the absolute error is lower than the defined boundary (indicated with P) was estimated. The results are indicated in Figure 16.

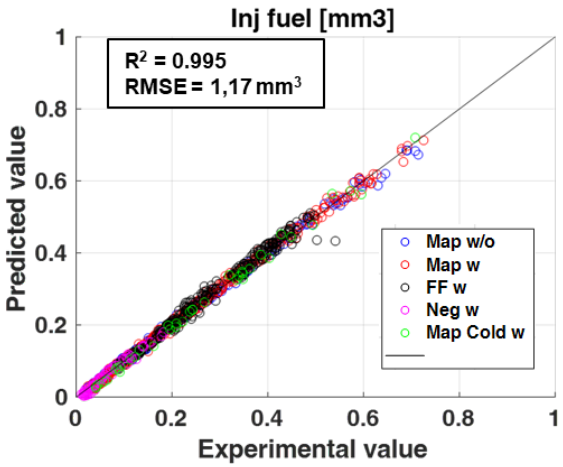

Figure 15. T2F NNRT model: predicted vs. experimental values of q_f for the steady-state test dataset.

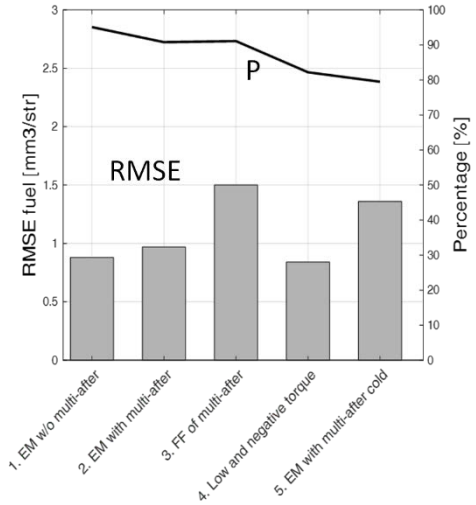

Figure 16. RMSE and P values of the T2F NNRT model, with reference to q_f estimation, for the different steady-state tests.

It can be seen, from Fig. 15, that the overall RMSE value is of the order of 1.2 mm^3. Moreover, the results reported in Fig. 16 indicate that the T2F NNRT model works correctly for all of the different types of tests.

Finally, the performance of the T2F NNRT model was also investigated under transient operation conditions. Figure 17 shows the RMSE and P values, concerning the q_f estimation from the T2F NNRT model for the different considered tests.

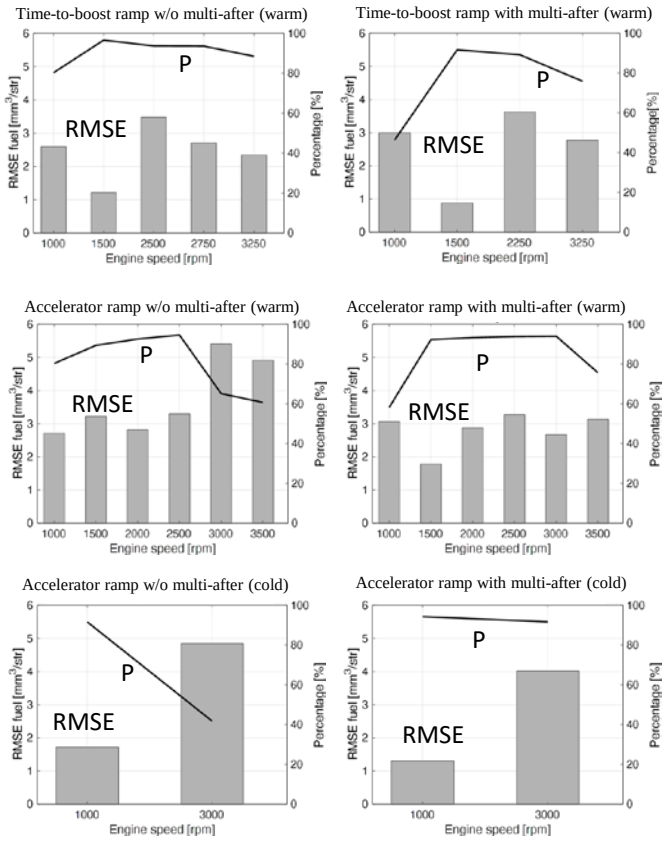

Figure 17. RMSE and P values of the T2F NNRT model, with reference to q_f estimation, over the different transient tests.

Figures 18-19 report a comparison of the predicted (blue line: T2F NNRT model) and experimental (red line: fuel from ECU, black line: fuel from test bench fuel meter) trends of q_f for the same transient tests considered for the F2T model. Moreover, the fuel quantity values in these figures were also normalized for confidentiality reasons. Figure 18 refers to the time-to-boost ramp at N=1500 rpm, while Fig. 19 refers to the accelerator pedal position ramp at N=3500 rpm. The upper and lower boundaries of q_f, which were defined in order to estimate the 'P' parameter in Fig. 17, are also reported in the figures with dashed red lines.

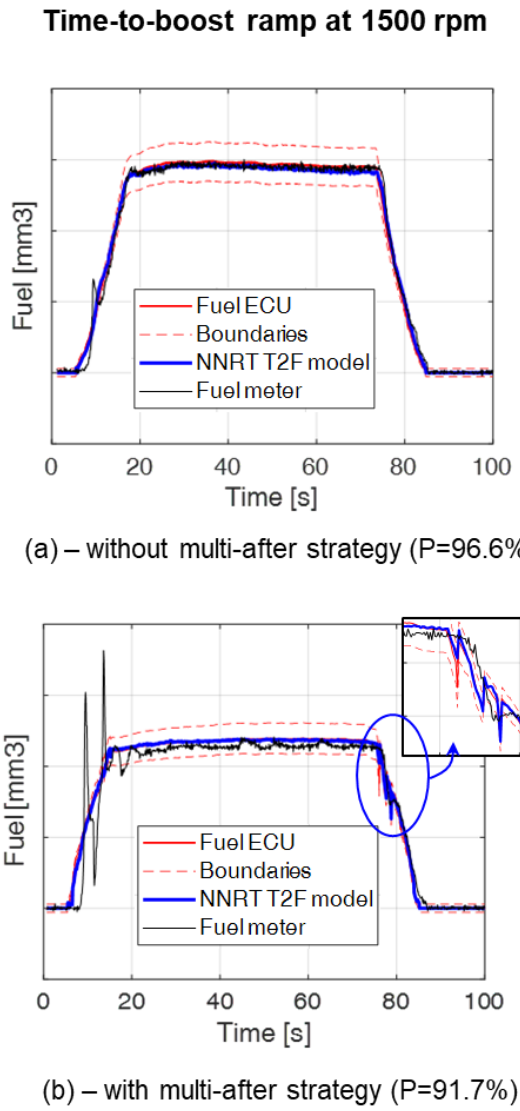

Figure 18. Experimental and predicted trends of q_f over the time-to-boost ramp at N=1500 rpm for test cases featuring combustion modes without (a) and with (b) multi-after injection strategies

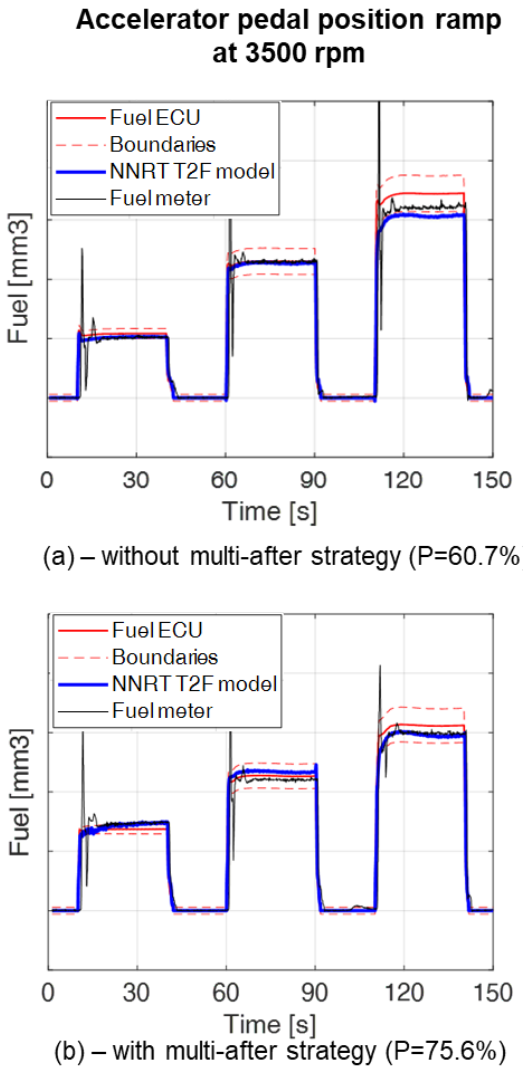

Figure 19. Experimental and predicted trends of q_f over an accelerator pedal position ramp at N=3500 rpm for test cases featuring combustion modes without (a) and with (b) multi-after injection strategies.

In general, the results of the T2F NNRT model are accurate for all the considered tests. It can also be seen that the fuel quantity provided by the T2F NNRT model is more in line with the fuel quantity estimated by the test bench fuel meter (black lines) than with the ECU fuel setpoint (red lines) over the steady-state intervals. This is a positive result, since the fuel derived from the test bench fuel meter is more accurate, at least under steady-state operation conditions. However, it can be seen in the figures that it is affected by high oscillations during the load ramps, due to a slow dynamic response.

It is also interesting to note, in Fig. 18b, that fuel oscillations (from both the ECU and NNRT model) occur during the down ramp, while the BMEP trend does not show these oscillations (see Fig. 12b). It was verified that these oscillations were mainly due to a change in injection strategy during this interval (i.e., number of after injections): in order to guarantee the same BMEP, it is in fact necessary to modify the total injection quantity, so as to compensate for the variations in the engine thermal efficiency, which occur when the injection strategy is changed. It should be highlighted that the ECU performs the fuel quantity correction by means of its internal torque-to-fuel maps (red lines), and the NNRT model (blue line) is able to reproduce this behaviour in a fully predictive way. This is a

confirmation of the capability of the NNRT model to adjust the fuel quantity in order to compensate for the variations of the engine efficiency, related to the variation of the injection strategy, in a similar way to that of the standard ECU software.

Finally, Fig. 20 plots a zoomed view of the transient tests reported in Figs. 18-19.

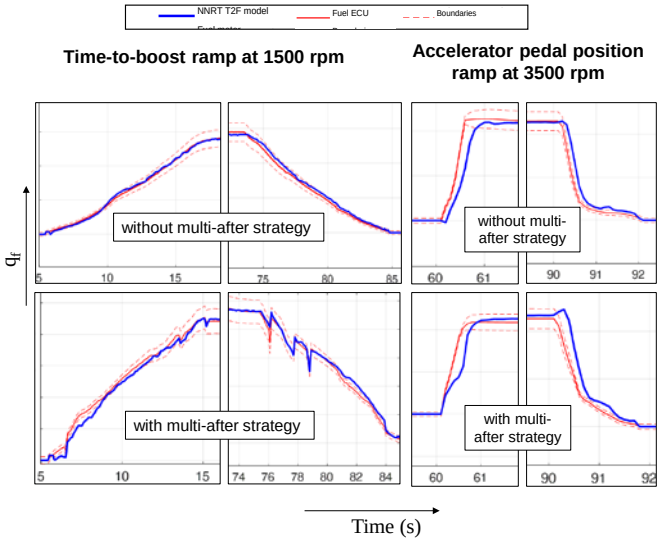

Figure 20. Zoomed view of the rising and descending edges of the transient tests shown in Figs. 18-19.

Computational time

The physical and NNRT models have already been compared in [10], in terms of computational time. It was shown in that study that the NNRT model is more computationally efficient than the physical model, as the required computational time is less than 10% of that of the physical model. Moreover, the number of neurons does not affect the computational time required by the NNRT model.

The T2F NNRT model, which can be potentially be used as a BMEP controller, does not require any iteration (as instead would be required for the inversion of the physical model), as the model is trained directly using the BMEP target as input, and the total injected quantity q_f is provided directly as a model output.

Future work

The T2F NNRT model developed in this study showed a good potential for identifying the optimal injected fuel quantity for a given BMEP target, regardless of the injection strategy which is adopted (i.e., with and without multi after pulses). However, an additional research activity is still needed, in order to implement the model on a rapid prototyping approach and test its functionalities on the real engine, by-passing the standard ECU functions. In this way it will be possible to verify and fix potential issues that could arise when the torque controller is implemented on the real engine.

Summary/Conclusions

A computationally fast model-based approach for the real-time control of BMEP (Brake Mean Effective Pressure) has been developed and assessed for a Euro 6 1.6L GM diesel engine. The controller provides the fuel quantity necessary to achieve a desired BMEP target. The engine features complex injection patterns, including pilot, main and multi-after.

The approach is based on the use of feed-forward ANNs (artificial neural networks), which have been trained using by means of virtual tests simulated by a previously developed low-throughput mean-value physical combustion model. The model has been referred to as “NNRT” (Neural Network-based Real-Time) and has the aim of replicating the outcomes of the physical combustion model, but with a much shorter computational time in view of its implementation on the engine control unit. In this study, the physical combustion model has been assessed for complex injection patterns, including not only pilot and main shots, but also multi-after pulses. It was found that it is capable of accurately simulating the complex patterns of heat release, heat release rate and in-cylinder pressure which occur when multi-after injection strategies are adopted. Two different versions of the NNRT model were realized, i.e., fuel-to-torque (F2T) and torque-to-fuel (T2F) models. The T2F version can be potentially used as a BMEP controller, since it provides the fuel quantity that has to be injected into the combustion chamber in order to achieve a desired BMEP (or torque) target, which is provided as input. The computational time required for the training of the NNRT models is of the order of 3h.

The F2T NNRT model and the physical combustion model were first applied under steady-state and transient operation conditions, and it was found that they provide similar performances. The average RMSE (Root Mean Square Error) for the estimation of BMEP is of the order of 0.35 bar, under steady-state operation conditions. The accuracy of the estimation of BMEP is variable under transient operating conditions, according to the specific test. However, the accuracy does not deteriorate when combustion modes featuring multi-after injection strategies are adopted. Moreover, it should be noted that the error may also be due to reasons other than the accuracy of the model, such as temporal shift errors in the model input quantities and/or deviations between the fuel quantity setpoint of the engine control unit, which is given to the models as input, and the real injected fuel quantity.

The T2F NNRT model has then been assessed for the same tests. It was found that the average RMSE value for the estimation of the fuel quantity is of the order of 1.2 mm^3 under steady-state operation conditions. Moreover, the fuel quantities provided by the T2F NNRT model for the transient tests are in line with the measured ones, and the RMSE values range from 1 to 5 mm^3/cyc.

References

1. Xue, X., Rutledge, J., “Potentials of Electrical Assist and Variable Geometry Turbocharging System for Heavy-Duty Diesel Engine Downsizing,” SAE Technical Paper 2017-01-1035, 2017, doi:10.4271/2017-01-1035.
2. Di Iorio, S., Beatrice, C., Guido, C., Napolitano, P. et al. , “Impact of Biodiesel on Particle Emissions and DPF Regeneration Management in a Euro5 Automotive Diesel Engine,” SAE Technical Paper 2012-01-0839, 2012, doi:10.4271/2012-01-0839.
3. D'Ambrosio, S., Gaia, F., Iemmolo, D., Mancarella, A. et al., “Performance and Emission Comparison between a Conventional Euro VI Diesel Engine and an Optimized PCCI Version and Effect of EGR Cooler Fouling on PCCI Combustion,” SAE Technical Paper 2018-01-0221, 2018, doi:10.4271/2018-01-0221.
4. D'Ambrosio, S., Ferrari, A., Mancarella, A., Mittica, A., “Effects of Rate-Shaped and Multiple Injection Strategies on Pollutant Emissions, Combustion Noise and Fuel Consumption

in a Low Compression Ratio Diesel Engine," *International Journal of Automotive Technology* 21(2020):197-214, doi:10.1007/s12239-020-0020-0.
5. D'Ambrosio, S., Ferrari, A., Mancarella, A., Mancò, S. et al., "Comparison of the emissions, noise, and fuel consumption comparison of direct and indirect piezoelectric and solenoid injectors in a low-compression-ratio diesel engine," *Energies* 12, no, 21(2019):4023, doi:10.3390/en12214023.
6. Ferrari, A., Mittica, A., Novara, C., Vento, O., et al., "Further assessment of the injected mass closed-loop control strategy in the design of innovative fuel injection systems," *AIP Conference Proceedings* Vol. 2191, 17 December 2019, Article number 020070, doi:10.1063/1.5138803.
7. Finesso, R., Marello, O., Misul, D., Spessa, E., et al., "Development and Assessment of Pressure-Based and Model-Based Techniques for the MFB50 Control of a Euro VI 3.0L Diesel Engine," *SAE Int. J. Engines* 10, no. 4 (2017):1538-1555, doi:10.4271/2017-01-0794.
8. Finesso, R., Hardy, G., Marello, O., Spessa, E., et al., "Model-Based Control of BMEP and NOx Emissions in a Euro VI 3.0L Diesel Engine," *SAE Int. J. Engines* 10, no. 5(2017):2288-2304, doi:10.4271/2017-24-0057.
9. Finesso, R., Marello, O., Spessa, E., "Development of a pressure-based technique to control IMEP and MFB50 in a 3.0L diesel engine," *Energy Procedia* 148 (2018):424-430, doi: 10.1016/j.egypro.2018.08.105.
10. Finesso, R., Spessa, E., Yang, Y., Conte, G., et al., "Neural-Network Based Approach for Real-Time Control of BMEP and MFB50 in a Euro 6 Diesel Engine," SAE Technical Paper 2017-24-0068, 2017, doi:10.4271/2017-24-0068.
11. Finesso, R., Hardy, G., Mancarella, A, Marello, O., et al., "Real-Time Simulation of Torque and Nitrogen Oxide Emissions in an 11.0 L Heavy-Duty Diesel Engine for Model-Based Combustion Control," *Energies* 12(2019):460, doi:10.3390/en12030460.
12. Cococcetta, F., Finesso, R., Hardy, G., Marello, O., et al., "Implementation and Assessment of a Model-Based Controller of Torque and Nitrogen Oxide Emissions in an 11 L Heavy-Duty Diesel Engine," *Energies* 12(2019):4704, doi: 10.3390/en12244704.
13. Hu, S., d'Ambrosio, S., Finesso, R., Manelli, A., et al., "Comparison of Physics-Based, Semi-Empirical and Neural Network-Based Models for Model-Based Combustion Control in a 3.0 L Diesel Engine," *Energies* 12(2019):3423, doi: 10.3390/en12183423.
14. Finesso R, Misul D, Spessa E, Venditti M., "Optimal Design of Power-Split HEVs Based on Total Cost of Ownership and CO2 Emission Minimization," *Energies* 11(2018):1705, doi: 10.3390/en11071705.
15. Finesso, R., Spessa, E., Venditti, M., "Layout design and energetic analysis of a complex diesel parallel hybrid electric vehicle," *Applied Energy* 134(2014):573-588, doi:10.1016/j.apenergy.2014.08.007.
16. Finesso, R., Spessa, E., Venditti, M., "Cost-optimized design of a dual-mode diesel parallel hybrid electric vehicle for several driving missions and market scenarios," *Applied Energy* 177(2016):366-383, doi:10.1016/j.apenergy.2016.05.080.
17. Bosch Press, "Breakthrough: new Bosch diesel technology provides solution to NOx problem," Bosch, accessed October 2020, https://www.bosch-presse.de/pressportal/de/en/breakthrough-new-bosch-diesel-technology-provides-solution-to-nox-problem-155524.html .
18. Rakopoulos, C., Giakoumis, E., "Review of Thermodynamic Diesel Engine Simulations under Transient Operating Conditions", SAE Technical Paper 2006-01-0884, 2006, doi:10.4271/2006-01-0884.
19. Finesso, R., Spessa, E., Yang, Y., "Development and Validation of a Real-Time Model for the Simulation of the Heat Release Rate, In-Cylinder Pressure and Pollutant Emissions in Diesel Engines," *SAE Int. J. Engines* 9(2016):322-341, doi:10.4271/2015-01-9044.
20. Catania, A.E., Finesso, R., Spessa, E., "Predictive zero-dimensional combustion model for DI diesel engine feed-forward control," *Energy Conversion and Management* 52, no.10(2011): 3159–3175, doi:10.1016/j.enconman.2011.05.003.
21. Asprion, J., Chinellato, O., Guzzella, L., "A fast and accurate physics-based model for the NOx emissions of Diesel engines," *Appl. Energy* 103(2013):221-233, doi:10.1016/j.apenergy.2012.09.038.
22. Asprion, J., Chinellato, O., Guzzella, L., "Optimisation-oriented modelling of the NOx emissions of a Diesel engine,"*Energ. Convers. Manage* 75(2013):61-73, doi:10.1016/j.enconman.2013.05.039.
23. Andersson, M., Johansson, B., Hultqvist, A., and Noehre, C., "A Predictive Real Time NOx Model for Conventional and Partially Premixed Diesel Combustion," SAE Technical Paper 2006-01-3329, 2006, doi: 10.4271/2006-01-3329.
24. Najafi, B., Faizollahzadeh Ardabili, S., Mosavi, A., Shamshirband, S., et al., "An Intelligent Artificial Neural Network-Response Surface Methodology Method for Accessing the Optimum Biodiesel and Diesel Fuel Blending Conditions in a Diesel Engine from the Viewpoint of Exergy and Energy Analysis," *Energies* 11(2018):860, doi:10.3390/en11040860.
25. Brusca, S., Lanzafame, R., and Messina, M., "A Combustion Model for ICE by Means of Neural Network," SAE Technical Paper 2005-01-2110, 2005, doi: 10.4271/2005-01-2110.
26. Bennett, C., Dunne, J.F., Trimby, S., Richardson, D., "Engine cylinder pressure reconstruction using crank kinematics and recurrently-trained neural networks," *Mechanical systems and signal processing* 85(2016):126-145, doi:10.1016/j.ymssp.2016.07.015.
27. Li, H., Butts, K., Zaseck, K., Liao-McPherson, D., et al., "Emissions Modeling of a Light-Duty Diesel Engine for Model-Based Control Design Using Multi-Layer Perceptron Neural Networks," SAE Technical Paper 2017-01-0601, 2017, doi:10.4271/2017-01-0601.
28. Johri, R., Salvi, A. and Filipi, Z., "Real-time Transient Soot and NOx Virtual Sensors for Diesel Engine Using Neuro-Fuzzy Model Tree and Orthogonal Least Squares," *Journal of Engineering for Gas Turbines and Power* 134(2012):092806, doi:10.1115/1.4006942.
29. Abdullah, U., "A parametric study for specific fuel consumption of an intercooled diesel engine using a neural network", *Fuel* 93(2012):189-199, doi: 10.1016/j.fuel.2011.11.004.
30. Janakiraman,V.M., Nguyen, X., Assanis, D., "Nonlinear identification of a gasoline HCCI engine using neural networks coupled with principal component analysis," *Applied soft computing* 13, no.5(2013):2375-2389, doi: 10.1016/j.asoc.2013.01.006.
31. Cay, Y., "Prediction of a gasoline engine performance with artificial neural network", *Fuel* 111(2016):324-331, doi: 10.1016/j.fuel.2012.12.040.
32. Çay, Y., Korkmaz, I., Çiçek, A., Kara, F., "Prediction of engine performance and exhaust emissions for gasoline and methanol using artificial neural network", *Energy* 50(2013):177-186, doi: 10.1016/j.energy.2012.10.052.
33. Çay, Y., Çiçek, A., Kara, F., Sağiroğlu, S.,"Prediction of engine performance for an alternative fuel using artificial neural network", *Applied thermal engineering* 37(2012):217-225, doi: 10.1016/j.applthermaleng.2011.11.019.
34. Brahma, I., He, Y., and Rutland, C., "Improvement of Neural Network Accuracy for Engine Simulations," SAE Technical Paper 2003-01-3227, 2003, doi:10.4271/2003-01-3227.

35. Chen, S. and Flynn, P., "Development of a Single Cylinder Compression Ignition Research Engine," SAE Technical Paper 650733, 1965, doi:10.4271/650733.

Definitions/Abbreviations

ANN	Artificial neural network
BMEP	Brake Mean Effective Pressure
CA	crank angle
CFD	Computer Fluid-Dynamics
c_p	specific heat at constant pressure
c_v	specific heat at constant volume
CNG	Compressed Natural Gas
DA	Dwell-angle
DoE	Design of experiment
DT	Dwell-time
ECU	Engine Control Unit
EGR	Exhaust Gas Recirculation
EOI	end of injection
EVO	Exhaust Valve Opening
F2T	Fuel-to-Torque
FMEP	Friction Mean Effective Pressure
GM	General Motors
GM-GPS	General Motors – Global Propulsion Systems
H_L	lower heating value of the fuel
HCCI	Homogeneous Charge Compression Ignition
IMEP	Indicated Mean Effective Pressure
IVC	Intake Valve Closing
K	combustion rate coefficient
m	mass
$\dot{m}_{f,inj}$	fuel injection rate
N	rotational speed of the engine
n	compression phase polytropic coefficient
n'	expansion phase polytropic coefficient
NN	Neural network
NNRT	Neural-network-based real-time model
O_2	intake charge oxygen concentration
p	pressure
p_{EMF}	exhaust manifold pressure
p_f	injection pressure
p_{IMF}	intake manifold pressure
PCCI	Premixed Charge Compresison Ignition
PFP	Peak firing pressure
pil	pilot injection
q	injected fuel volume quantity
Q_{ch}	chemical heat release
$Q_{f,evap}$	energy associated with fuel evaporation
Q_{fuel}	chemical energy associated with the injected fuel
$Q_{ht,glob}$	global heat transfer between the charge and the walls
Q_{net}	net heat release
q_{aft}	injected fuel volume quantity of the after injection
q_f	total injected fuel volume quantity
q_{main}	injected fuel volume quantity of the pilot injection

q_{pil}	injected fuel volume quantity of the pilot injection
R^2	squared correlation coefficient
RDE	Real Driving Emission
RMSE	root mean square error
SOC	start of combustion
SOI	electric start of Injection
SVM	Support vector machine
t	time
T	temperature
T2F	Torque-to-Fuel
T_{IMF}	intake manifold temperature
V	volume
V2X	vehicle-to-everything technology
VGT	Variable Geometry Turbocharger

Greek symbols

$\gamma = c_p/c_v$	specific heat ratio
ρ	density
ρ_{SOI}	in-chamber ambient density evaluated at the SOI instant
ρ_{SOC}	in-chamber ambient density evaluated at the SOC instant
τ_{aft}	ignition delay of the after pulse
τ_{main}	ignition delay of the main pulse
τ_{pil}	ignition delay of the pilot pulse